Chinese Chemical Letters 34 (2023) 108291

Contents lists available at ScienceDirect

Chinese Chemical Letters

journal homepage: www.elsevier.com/locate/cclet

Ultrafine Co nanoparticles confined in nitrogen-doped carbon toward two-electron oxygen reduction reaction for H_2O_2 electrosynthesis in acidic media

Xiaoqing Cui[a], Lijie Zhong[a,*], Xu Zhao[b], Jingxin Xie[a], Dequan He[a], Xin Yang[a], Kanglong Lin[a], Huan Wang[a], Li Niu[a,*]

[a] Guangdong Engineering Technology Research Center for Sensing Materials & Devices, Guangzhou Key Laboratory of Sensing Materials & Devices, Center for Advanced Analytical Science, School of Chemistry and Chemical Engineering, School of Civil Engineering, Guangzhou University, Guangzhou 510006, China
[b] Key Laboratory of Drinking Water Science and Technology, Research Center for Eco-Environmental Sciences, Chinese Academy of Sciences, Beijing 100085, China

ARTICLE INFO

Article history:
Received 5 October 2022
Revised 2 February 2023
Accepted 2 March 2023
Available online 12 March 2023

Keywords:
Oxygen reduction reaction
H_2O_2 production
Confined Co nanoparticles
Electrocatalysis
Acidic media

ABSTRACT

Electrocatalytic production of hydrogen peroxide (H_2O_2) by two-electron oxygen reduction reaction (2e⁻ ORR) under acidic condition has been considered to have great application value. Co nanoparticles (CoNPs) coupled with N-doped carbon are a class of potential electrocatalysts. The effective strategies to further enhance their performances are to improve the active sites and stability. Herein, the material containing ultrafine CoNPs confined in a nitrogen-doped carbon matrix (NC@CoNPs) was synthesized by pyrolyzing corresponding precursors, which was obtained through regulating the topological structure of ZIF-67/ZIF-8 with dopamine (DA). The DA self-polymerization process induced the formation of CoNPs with smaller sizes and formed polydopamine film decreased the detachment of CoNPs from the catalyst. High density of Co-N_x active sites and defective sites could be identified on NC@CoNPs, leading to high activity and H_2O_2 selectivity, with an onset potential of 0.57 V (*vs.* RHE) and ~90% selectivity in a wide potential range. An on-site electrochemical removal of organic pollutant was achieved rapidly through an electro-Fenton process, demonstrating its great promise for on-site water treatment application.

Hydrogen peroxide (H_2O_2), as one of the 100 most important chemicals in the world, has been widely used in the treatment of wastewater, disinfection, bleaching of textile and pulp fields [1–3]. Currently more than 95% H_2O_2 was produced through the centralized multi-step anthraquinone process, and then diluted and transported to the location where H_2O_2 was needed, leading to the storage and transport costs [4]. The electrocatalytic production of H_2O_2 through two-electron oxygen reduction reaction (2e⁻ ORR) offer small-scale, on-site synthesis of dilute H_2O_2, which is suitable for many distributed applications including water treatment and disinfection [5–7]. This method for H_2O_2 production was firstly reported by Berl in 1930 and attracted increasing attention in recent years with the development of ORR catalysts [8–10]. Electrocatalytic H_2O_2 production could proceed in acidic, neutral or basic electrolytes, and acidic environment is particularly attractive due to the decomposition of H_2O_2 in alkaline environment [11]. The key challenge here is to develop robust ORR electrocatalysts featuring high activity, selectivity and stability toward the 2e⁻ ORR pathway in acidic media.

A few catalysts have been reported for 2e⁻ ORR toward electrosynthesis of H_2O_2, typically including metal-free carbon materials, precious metal-based catalysts, transition metal-based materials. The ORR activity of metal-free carbon materials is relatively low due to their weak adsorption toward reaction intermediate, although their activities could be modulated by complex heteroatomic doping and pore engineering [12–16]. For noble-metal based catalysts, it has demonstrated that the ORR selectivity could be shifted from 4e⁻ to 2e⁻ pathway through alloying [17–19], poisoning [20,21] and single atomic engineering [22]. However, the cost remains a consideration upon practical application and the stability for single atomic catalyst (SACs) is either an issue. Transition metal-based materials have been also investigated for electrochemical H_2O_2 production, including NiS_2 nanosheets [23], α-Fe_2O_3 single crystals with exposed [001] facet [24], plasma-induced defective TiO_{2-x} [25], Co-tetramethoxyphenylporphyrin/carbon nanotube (CoTMPP/CNT) nanohybrid [26], CoS_2 [27], $CoSe_2$ [28] and Co-based SACs (CoSACs)

* Corresponding authors.
E-mail addresses: ccljzhong@gzhu.edu.cn (L. Zhong), lniu@gzhu.edu.cn (L. Niu).

https://doi.org/10.1016/j.cclet.2023.108291
1001-8417/

[29–32]. Among these, Co-based materials are the focused electrocatalysts considering optimal binding strength to the reaction intermediate of *OOH, which is an effective factor to determine the activity of $2e^-$ ORR. For example, Sun *et al.* reported nitrogen-doped carbon materials containing atomically dispersed $M-N_x$ sites (M = Co, Ni, Fe, Cu and Mn) for H_2O_2 production in acidic media, and the material containing $Co-N_x$ sites exhibited high selectivity of 80% [31]. Dong *et al.* synthesized MTMPP (M = Mn, Fe, Co, Ni and Cu)/CNT catalysts for electrochemical synthesis of H_2O_2, and CoTMPP/CNT hybrid demonstrated the best $2e^-$ ORR activity compared with other MTMPP/CNT catalysts [26]. However, some issues remain for these materials. For example, the CoS_2 [27] and $CoSe_2$ [28] only disclose high selectivity for $2e^-$ ORR in a narrow potential range (at high potentials). CoSACs, typically Co-N-C materials exhibit high activity and stability in alkaline media but face challenges in acidic media [32].

Upon these considerations, we prepared ultrafine Co nanoparticles (CoNPs) confined in a nitrogen-doped carbon matrix (NC@CoNPs) through pyrolysis of polydopamine (PDA)@ZIF-67/ZIF-8. ZIF-67 consisted of 2-methylimidazole and Co^{2+} ion in the form of tetrahedral ordered structure, and ZIF-8 has a similar structure as ZIF-67 but with different metal center of Zn^{2+} ion [33,34]. The two different metals compete for the ligand and thus improve the dispersity for the obtained CoNPs. Zn^{2+} was finally removed by evaporation at high temperature (boiling point ≈ 907 °C). Meanwhile, the self-polymerization process of dopamine (DA) induced the formation of ultrafine and dispersed CoNPs and the nitrogen-doped carbon film derived from PDA further acted as the protective layer for CoNPs. The obtained NC@CoNPs presented approximate 90% selectivity in acidic media as well as good stability over 20 h electrolysis. The catalyst was effective for rapid degradation of rhodamine B (RhB) through electro-Fenton process, demonstrating its promising application in waste water treatment.

The N-doped carbon confined CoNPs (NC@CoNPs) was synthesized as shown in Fig. 1a. Firstly, the self-polymerization process of DA was proceeded during the growth of ZIF-67/ZIF-8 to obtain the precursor of PDA@ZIF-67/ZIF-8. Then the PDA@ZIF-67/ZIF-8 was converted to NC@CoNPs through high temperature calcination and acid washing treatment. For comparison, the N-doped carbon supported CoNPs (NC/CoNPs) was prepared with the same procedure but without dopamine introduced (Fig. 1b). The chemical compositions of NC@CoNPs and NC/CoNPs were first characterized by X-ray diffraction (XRD), which showed the presence of graphite carbon and metallic Co for both materials and no characteristic peaks related to other metal phases were observed (Fig. 1c). The peak intensity of NC@CoNPs was weaker than NC/CoNPs for C (002) at $2\theta = 26^o$, suggesting lower crystallinity of carbon matrix for NC@CoNPs [7,35]. The morphologies and structures of the materials were further characterized by scanning electron microscopy (SEM) and transmission electron microscopy (TEM). The SEM image of NC@CoNPs (Fig. 1d) presented the structure of carbon clusters while that of NC/CoNPs (Fig. 1e) showed the sheet structure. The XRD patterns of N-doped carbon (NC) show two characteristic peaks of graphite carbon (Fig. S1a in Supporting information) and no any metal phases observed, which was consistent with the TEM image of NC (Fig. S1b in in Supporting information).

Fig. 2a provides the TEM image of NC@CoNPs and corresponding EDS mapping results, which discloses the presence of carbon matrix confined and embedded CoNPs with size of about 15 nm and the elements of N, O and Co were uniformly distributed within the carbon matrix. Moreover, the pore structures could also be observed from the TEM image, which is advantageous for the mass transfer during ORR process [15]. High-resolution TEM (HRTEM) analysis displayed the nanoparticle contained (111) facet of metallic Co phase with lattice spacing of 0.196 nm (Fig. 2b), which coincided with the XRD results. Differently, the TEM image of NC/CoNPs showed the CoNPs with size of above 100 nm loaded on the carbon sheets (Fig. 2c). These suggested that the presence of DA self-polymerization process in the synthesis process induced the formation of carbon clusters with ultrafine and embedded CoNPs.

The defect degree of the materials was examined by Raman spectra (Fig. 2d) with typical D band (1347 cm^{-1}) and G band (1591 cm^{-1}). D band was related with the vacancies or defects

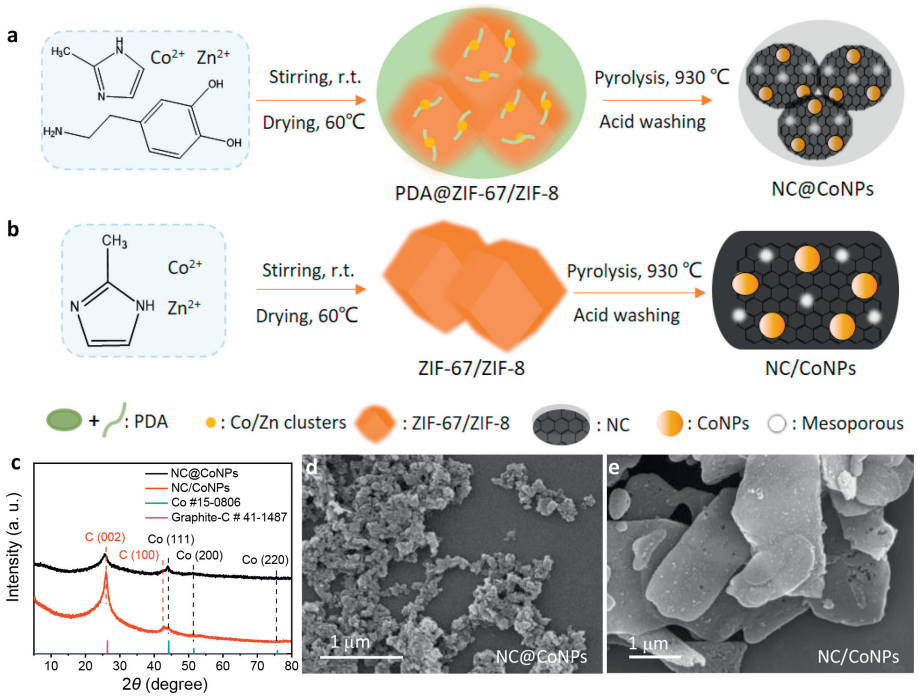

Fig. 1. Preparation of N-doped carbon confined CoNPs (NC@CoNPs) and supported CoNPs (NC/CoNPs). (a, b) The synthesis routes for NC@CoNPs and NC/CoNPs. (c) XRD patterns of NC@CoNPs and NC/CoNPs. (d, e) SEM images of NC@CoNPs and NC/CoNPs.

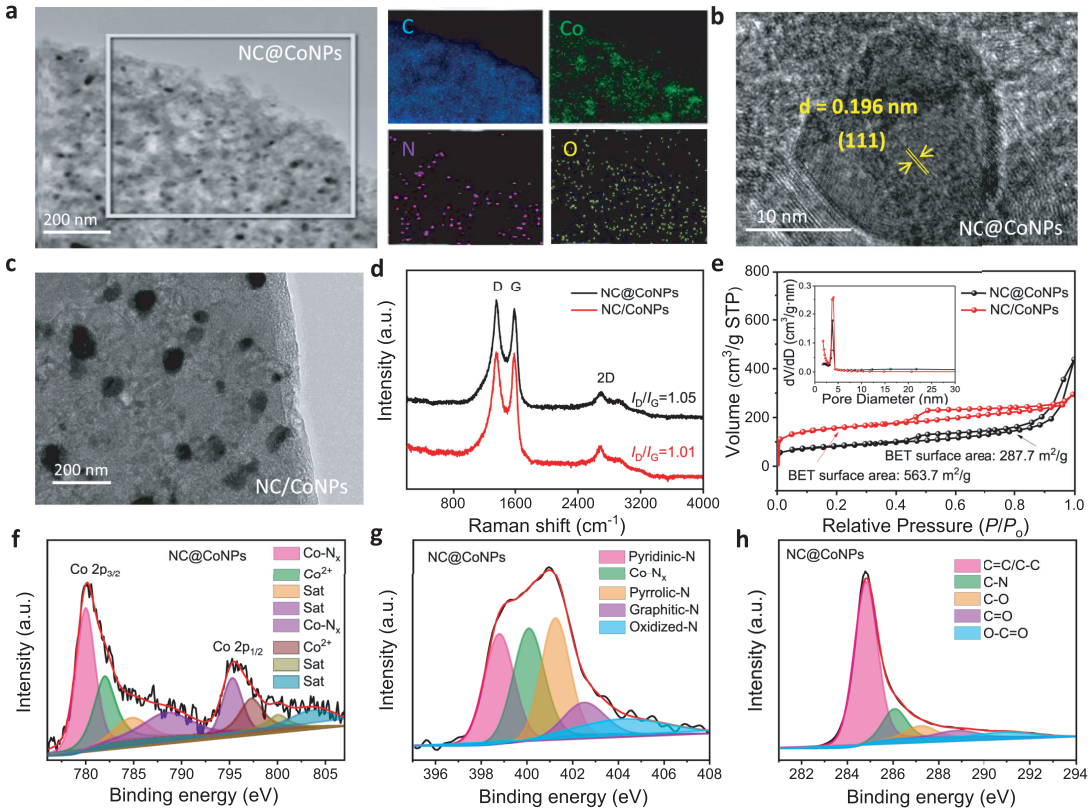

Fig. 2. Structure and composition of catalysts. (a) TEM image of NC@CoNPs and corresponding EDS-mapping. (b) High-resolution TEM image of NC@CoNPs. (c) TEM image of NC/CoNPs. (d) Raman spectra of NC@CoNPs and NC/CoNPs. (e) N_2 adsorption–desorption isotherms and pore size distribution (the insert) for NC@CoNPs and NC/CoNPs. High-resolution XPS spectra of (f) Co 2p (g) N 1s and (h) C 1s of NC@CoNPs.

and G band was originated from in-plane vibration of sp^2 carbon atoms. The D/G intensity ratios of NC@CoNPs ($I_D/I_G = 1.05$) increased compared with that of NC/CoNPs ($I_D/I_G = 1.01$), suggesting more defective sites for NC@CoNPs. The defect favored the improvement of ORR activity and H_2O_2 selectivity [36,37]. Fig. 2e showed the N_2 adsorption–desorption isotherms of NC@CoNPs and NC/CoNPs. The clear hysteresis loops ($0.42 < P/P_0 < 0.98$) belong to the type IV adsorption isotherms, and the pore size of 3.8 nm was observed, indicating the presence of mesoporous structures [15,38]. The Brunner-Emmett-Teller (BET) surface area of NC@CoNPs (287.7 m^2/g) was lower than that of NC/CoNPs (563.7 m^2/g), which is reasonable since CoNPs was confined in NC layer. The mesoporous structures were believed to benefit the release of H_2O_2 from the catalyst during reaction [39].

XPS was further employed to analyze the surface chemical composition. Fig. S2 and Fig. S3a (Supporting information) provided the survey spectra of NC@CoNPs and NC/CoNPs, respectively. There were four kinds of elements of Co, N, C and O present for both catalysts, and the Co atomic percentages were 0.52% for NC@CoNPs and 0.37% for NC/CoNPs, respectively. The increased Co atomic percentage of NC@CoNPs could be related with the fact that CoNPs were embedded in the N-doped carbon layers and not easily removed through acid washing treatment. Fig. 2f showed high-resolution Co 2p spectrum of NC@CoNPs, which contained two regions of $2p_{1/2}$ and $2p_{3/2}$. Each region was fitted with two main peaks and two satellite peaks. The two main peaks in the Co $2p_{3/2}$ region were at 780 and 782 eV, which could be assigned to Co–N_x and Co^{2+} moieties [7,31,40]. The Co–N_x active sites were expected to favor the ORR activity and H_2O_2 selectivity [7,31]. Specially, the higher Co atomic percentage and smaller size of CoNPs would result in the increase of Co–N_x active sites. High-resolution N 1s spectrum of NC@CoNPs could be deconvoluted into five components (Fig. 2g), which belonged to different nitrogen electronic environments, including pyridinic–N (398.8 eV), Co–N_x (400.1 eV), pyrrolic–N (401.3 eV), graphitic–N (403 eV), and N–oxide (404.8 eV) [31,41]. The high-resolution C 1s spectrum of NC@CoNPs (Fig. 2h) was fitted into five peaks located between 284.8 eV and 290.5 eV, which assigned to C=C/C-C, C-N, C-O, C=O and O-C=O [2], respectively. Figs. S3b-d (Supporting information) showed the high-resolution Co 2p, N 1s and C 1s spectra of NC/CoNPs. The ratio of pyrrolic–N/pyridinic–N decreased for NC/CoNPs compared with that of NC@CoNPs, which was consistent with the decreased Co atomic percentage of NC/CoNPs. Thus, it could be deduced that the Co is most likely coordinated with pyrrolic N.

The electrochemical features of NC@CoNPs and NC/CoNPs were first characterized by cyclic voltammetry in Ar-saturated 0.1 mol/L $HClO_4$ (Fig. 3a). The capacitive current of NC@CoNPs was higher than that of NC/CoNPs, suggesting better electron storage performance of NC@CoNPs. A pair of reversible redox peaks at approximately 0.45 V (*vs.* RHE) was observed for NC/CoNPs, which could be assigned to the redox reaction of Co(II)/Co(III). The ORR performance was examined through rotating-ring-disk-electrode (RRDE) voltammograms in O_2-saturated 0.1 mol/L $HClO_4$ at a scan rate of 10 mV/s, and the potential on the platinum ring was fixed at 1.25 V (*vs.* RHE). Fig. 3b showed the RRDE voltammograms of NC@CoNPs with different mass loadings. The loading of 0.4 mg/cm^2 exhibited optimal H_2O_2 activity and selectivity (Figs. 3b and c). Therefore, the loading of 0.4 mg/cm^2 was used throughout the experiment. Fig. 3d presented the RRDE voltammograms of the materials, and the ORR onset potentials (at 0.1 mA/cm^2) of 0.57 V and 0.66 V (*vs.* RHE) were obtained for NC@CoNPs and NC/CoNPs, respectively. For NC@CoNPs, the H_2O_2 selectivity was ~90% over a wide range of potentials, which is better than that of NC/CoNPs (Fig. 3e).

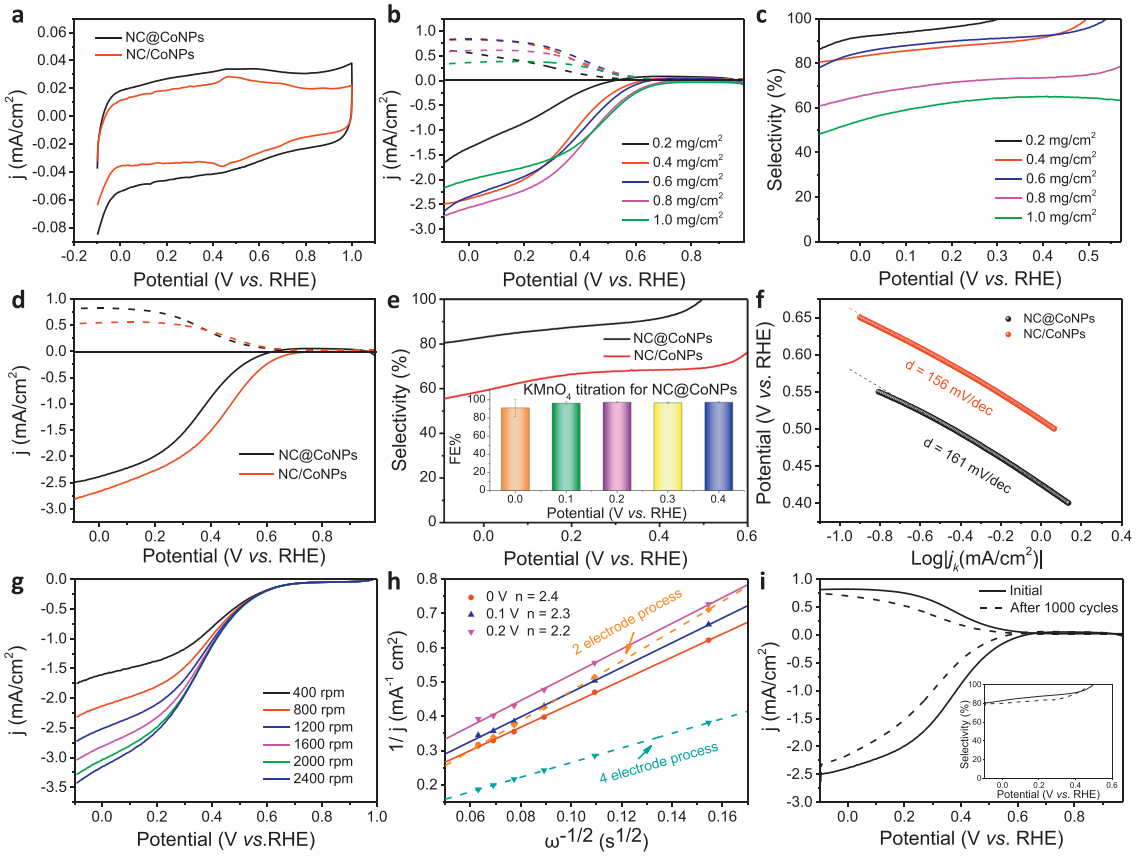

Fig. 3. Electrochemical ORR tests. (a) CVs of NC@CoNPs and NC/CoNPs in Ar-saturated 0.1 mol/L $HClO_4$ at a scan rate of 10 mV/s. (b) RRDE polarization curves of NC@CoNPs catalyst with different loadings in O_2-saturated 0.1 mol/L $HClO_4$ and (c) corresponding H_2O_2 selectivity. (d) RRDE polarization curves of NC@CoNPs and NC/CoNPs catalyst with the loading of 0.4 mg/cm^2 in O_2-saturated 0.1 mol/L $HClO_4$ and (e) corresponding H_2O_2 selectivity; The inset: the H_2O_2 Faradaic efficiency for NC@CoNPs by $KMnO_4$ titration under electrolysis at different potentials. (f) Tafel plots for NC@CoNPs and NC/CoNPs. (g) RRDE polarization curves of NC@CoNPs at different rotating speeds in O_2-saturated 0.1 mol/L $HClO_4$, and (h) corresponding Koutecky–Levich (K-L) plots at different potentials derived from RRDE measurements. (i) RRDE voltammograms of NC@CoNPs before and after 1000 cyclic tests. The inset showed the corresponding H_2O_2 selectivity.

The Faradaic of H_2O_2 (FE%) was further evaluated through electrolysis experiment. The inset in Fig. 3e showed that the calculated H_2O_2 FE% of NC@CoNPs was all above 90% at different potentials with the maximum value of 95% at 0.2 V and 0.4 V, which is also better than reported Co-based 2e$^-$ ORR catalysts [27,28,32]. Both NC@CoNPs and NC/CoNPs disclose a high Tafel slope of 161 mV/dec and 156 mV/dec, respectively (Fig. 3f), indicating the controlling step toward the formation of *OOH.

The electron transfer numbers of NC@CoNPs were further calculated with Koutecky–Levich (K–L) equation based on the RRDE voltammograms at different rotating speeds (Fig. 3g), and the results showed that the numbers at different potentials were all close to 2 ($n = 2.2$–2.4) (Fig. 3h), consistent with the result from H_2O_2 selectivity. According to many of reported literatures about Co-based materials, the H_2O_2 selectivity was mostly related with the density of Co–N_x active sites or defective sites, the distribution of N types with different electronic environments, and the porosity structure [7,12,42]. The materials of NC@CoNPs and NC/CoNPs presented similar distribution of N types and porosity structure, but the density of Co–N_x active sites and defective sites of NC@CoNPs was superior to that of NC/CoNPs, leading to higher H_2O_2 selectivity. Then the stability of NC@CoNPs was initially checked through an accelerated durability test (ADT) by continuously sweeping the RRDE voltammograms for 1000 cycles, as shown in Fig. 3i. The RRDE voltammograms show a certain potential shift, which is possibly due to the falling off the catalyst from the electrode but the H_2O_2 selectivity obtained before and after ADT was nearly not changed (the inset of Fig. 3i), indicating relatively stability of NC@CoNPs. Overall, we have demonstrated that the confined NC@CoNPs could regulate the ORR from 4e$^-$ to 2e$^-$ and exhibit a high H_2O_2 selectivity nearly in a whole potential range.

Then the stability of NC@CoNPs was further assessed through the steady-state current test at 0.2 V (*vs.* RHE) over 20 h. The result shows that the current value drops a little at first, and then stabilized over time (Fig. S4a in Supporting information). The dissolution of Co during the test was determined to be 2.3 μg/L by inductively coupled plasma-atomic emission spectroscopy test. H_2O_2 FE% retained nearly unchanged before and after the test (Fig. S4b in Supporting information). Moreover, the TEM images disclose no apparent morphology change for NC@CoNPs before and after the test (Fig. S5 in Supporting information). Table S1 (Supporting information) lists the performance comparison of NC@CoNPs catalyst and other 2e$^-$ ORR catalysts in acidic media, demonstrating the advantages of NC@CoNPs for 2e$^-$ ORR process.

The flow cell test was also carried out to evaluate the H_2O_2 production ability of NC@CoNPs in 0.1 mol/L $HClO_4$ as shown in Fig. S6a (Supporting information). As observed, the concentration of produced H_2O_2 linearly increases with the reaction time, indicating a constant rate of peroxide formation. For even longer duration, the increase rate of H_2O_2 slows down and the H_2O_2 FE% decreased (Fig. S6b in Supporting information), indicating a decreasing rate of peroxide production. This is related with the fact that the increasing concentration of peroxide in the electrolyte leads to increased reaction rate of peroxide reduction.

Subsequently, the influence of different pH conditions for the performances of NC@CoNPs was investigated. As seen in Fig. 4a,

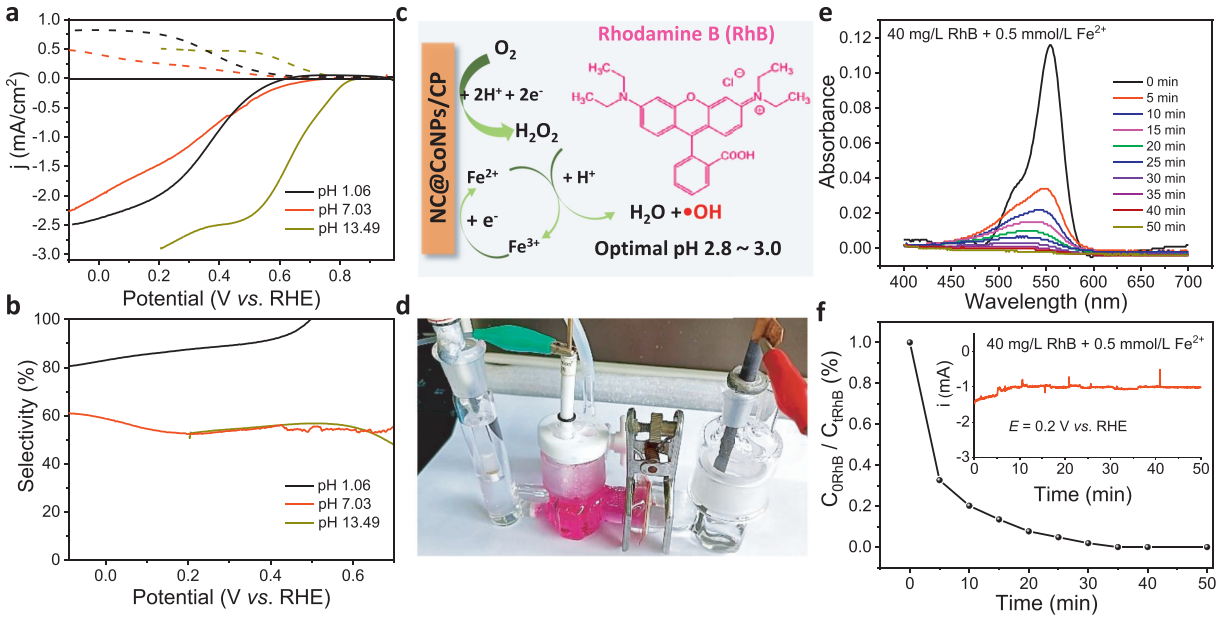

Fig. 4. (a) RRDE polarization curves of NC@CoNPs catalyst with the loading of 0.4 mg/cm^2 and (b) corresponding H_2O_2 selectivity in O_2-saturated 0.1 mol/L $HClO_4$ (pH 1.06), 0.1 mol/L Na_2SO_4 (pH 7.03), and 0.1 mol/L KOH (pH 13.49). (c) A schematic illustration and (d) the photograph of the electro-Fenton process based on NC@CoNPs in O_2-saturated electrolyte containing 0.5 mmol/L Fe^{2+}, pH 2.93 (initial concentration of RhB is 40 mg/L). (e) UV-vis absorption spectra for monitoring the electro-Fenton degradation process of 40 mg/L RhB solutions. (f) Decays of the concentration of RhB during electro-Fenton process. Insert: Chronoamperometry curve of electro-Fenton process at 0.2 V (*vs.* RHE).

the ORR onset potentials of 0.81, 0.64 and 0.57 V (*vs.* RHE) were obtained for pH 13.49, pH 7.03 and pH 1.06, respectively. The H_2O_2 selectivity was in the following order of pH 1.06 (~90%) > pH 13.49 (~50%) = pH 7.03 (~50%) (Fig. 4b). The pH dependence was also observed for other reported non-noble metal-nitrogen-carbon catalysts in previous reports [11,31], which might be related with the participation of proton in the reaction process.

For comparison, the ORR performances of NC were also examined in different pH conditions through RRDE voltammograms as shown in Fig. S7a (Supporting information), which all present low selectivity (Fig. S7b in Supporting information). This results further confirms the crucial role of Co–N_x active sites in NC@CoNPs for 2e$^-$ ORR performance.

The H_2O_2 could be used to remove organic pollutants through an electro-Fenton process, which was based on the following equations:

$$Fe^{2+} + H_2O_2 + H^+ \rightarrow Fe^{3+} + H_2O + {}^{\bullet}OH \quad (1)$$

$$Fe^{3+} + e^- \rightarrow Fe^{2+} \quad (2)$$

The reaction between H_2O_2 and Fe^{2+} can produce hydroxyl radical ($^{\bullet}OH$) (Eq. 1), which is a kind of powerful oxidant used to degrade common persistent organic pollutants. In this electro-Fenton process, H_2O_2 is electrogenerated from 2e$^-$ ORR at the cathode, while Fe^{2+} is rapidly regenerated from the reduction of Fe^{3+} (Eq. 2) at the same cathode (Fig. 4c). This leads to the rapid production of $^{\bullet}OH$ when compared to the conventional chemical Fenton process. Moreover, the electro-Fenton process proceed at an optimal acidic pH of 2.8–3.0. Therefore, the 2e$^-$ ORR performances of NC@CoNPs were also examined in this pH condition (pH 2.93) as shown in Fig. S8a (Supporting information), in which a satisfactory selectivity was obtained (~80% at 0.2 V, Fig. S8b in Supporting information). Then, we carried out the electro-Fenton degradation tests with RhB as a model organic pollutant (Fig. 4d). Electro-Fenton degradation tests were performed at room temperature in O_2-saturated acidified 0.1 mol/L Na_2SO_4 solution (pH 2.93) with the presence of both RhB (40 mg/L) and Fe^{2+} (0.5 mmol/L) in a three-electrode H-cell setup using NC@CoNPs as the working cathode operated at 0.2 V (*vs.* RHE). The UV-vis absorption spectrum was used to monitor the organic dye concentration as a function of time during each test (Fig. 4e). The overall catalytic current remained steady regardless of the decay of the RhB concentration over time (Fig. 4f), suggesting that RhB was degraded *via* the electro-Fenton process rather than the direct electrochemical destruction on the cathode. Significantly, the RhB completely degraded and decolored within a short period of 30 min. The result demonstrated the potential ability of NC@CoNPs in electro-Fenton process and water treatment applications due to its good performance toward electrochemical H_2O_2 production in acidic condition.

In summary, we synthesized the 2e$^-$ ORR catalyst of NC@CoNPs by simply carbonizing a self-assembled precursor of PDA@ZIF-67/ZIF-8. Detailed structural characterizations demonstrated that NC@CoNPs featured ultrafine CoNPs confined in nitrogen-doped carbon clusters, and high density of Co–N_x active sites and defective sites could be identified. The role of PDA was investigated in detail. This method emphasized the DA self-polymerization process regulated the size and dispersity of CoNPs, and the formed PDA inhibited the detachment of CoNPs from the catalyst. RRDE and electrolysis experiments showed that NC@CoNPs presented rapid ORR kinetics and superior H_2O_2 selectivity in a wide potential range. Such robust H_2O_2 production allows for the effective electro-Fenton process on the NC@CoNPs electrode and the efficient degradation of a model organic pollutant, demonstrating the high performance of NC@CoNPs to act as the 2e$^-$ ORR catalyst.

Declaration of competing interest

The authors declare that they have no known competing financial interests or personal relationships that could have appeared to influence the work reported in this paper.

Acknowledgments

This work has received financial support from the Natural Science Foundation of China (Nos. 21805052 and 2278092), Science and Technology Research Project of Guangzhou (Nos. 202102020787 and 202201000002), Department of Science & Technology of Guangdong Province (ID: 2022A156), Key Discipline of Materials Science and Engineering, Bureau of Education of Guangzhou (No. 20225546) and the Innovation & Entrepreneurship for the College Students of Guangzhou University (No. XJ202111078175).

Supplementary materials

Supplementary material associated with this article can be found, in the online version, at doi:10.1016/j.cclet.2023.108291.

References

[1] Z. Bao, J. Zhao, S. Zhang, et al., J. Mater. Chem. A 10 (2022) 4749–4757.
[2] H.W. Kim, M.B. Ross, N. Kornienko, et al., Nat. Catal. 1 (2018) 282–290.
[3] Y. Yi, L. Wang, G. Li, H. Guo, Catal. Sci. Technol. 6 (2016) 1593–1610.
[4] X.L. Zhang, X. Su, Y.R. Zheng, et al., Angew. Chem. Int. Ed. 60 (2021) 26922–26931.
[5] Z. Li, A. Kumar, N. Liu, et al., J. Mater. Chem. A 10 (2022) 14355–14363.
[6] L. Jing, Q. Tian, P. Su, et al., J. Mater. Chem. A 10 (2022) 4068–4075.
[7] B.S. Rawah, W. Li, Chin. J. Catal. 42 (2021) 2296–2305.
[8] N. Wang, S. Ma, P. Zuo, J. Duan, B. Hou, Adv. Sci. 8 (2021) 2100076.
[9] S. Yang, A. Verdaguer-Casadevall, L. Arnarson, et al., ACS Catal. 8 (2018) 4064–4081.
[10] Y. Jiang, P. Ni, C. Chen, et al., Adv. Energy Mater. 8 (2018) 1801909.
[11] J.Y. Zhang, C. Xia, H.F. Wang, C. Tang, J. Energy Chem. 67 (2022) 432–450.
[12] D. Iglesias, A. Giuliani, M. Melchionna, et al., Chem 4 (2018) 106–123.
[13] Y. Sun, I. Sinev, W. Ju, et al., ACS Catal. 8 (2018) 2844–2856.
[14] Y. Pang, K. Wang, H. Xie, et al., ACS Catal. 10 (2020) 7434–7442.
[15] L. Jing, C. Tang, Q. Tian, et al., ACS Appl. Mater. Interface 13 (2021) 39763–39771.
[16] S. Xu, Y. Gao, T. Liang, L. Zhang, B. Wang, Chin. Chem. Lett. 33 (2022) 5152–5157.
[17] J.S. Jirkovsky, I. Panas, E. Ahlberg, et al., J. Am. Chem. Soc. 133 (2011) 19432–19441.
[18] S. Siahrostami, A. Verdaguer-Casadevall, M. Karamad, et al., Nat. Mater. 12 (2013) 1137–1143.
[19] A. Verdaguer-Casadevall, D. Deiana, M. Karamad, et al., Nano Lett. 14 (2014) 1603–1608.
[20] D. He, L. Zhong, S. Gan, et al., Electrochim. Acta 371 (2021) 137721.
[21] L. Zhong, D. He, J. Xie, et al., Chem. Eng. J. 435 (2022) 135105.
[22] J. Liu, Z. Gong, M. Yan, et al., Small 18 (2022) 2103824.
[23] J. Liang, Y. Wang, Q. Liu, et al., J. Mater. Chem. A 9 (2021) 6117–6122.
[24] R. Gao, L. Pan, Z. Li, et al., Adv. Funct. Mater. 30 (2020) 1910539.
[25] K. Dong, J. Liang, Y. Wang, et al., Chem. Catal. 1 (2021) 1437–1448.
[26] K. Dong, J. Liang, Y. Ren, et al., J. Mater. Chem. A 9 (2021) 26019–26027.
[27] H. Sheng, E.D. Hermes, X. Yang, et al., ACS Catal. 9 (2019) 8433–8442.
[28] H. Sheng, A.N. Janes, R.D. Ross, et al., Energy Environ. Sci. 13 (2020) 4189–4203.
[29] C. Tang, L. Chen, H. Li, et al., J. Am. Chem. Soc. 143 (2021) 7819–7827.
[30] J. Gao, H.B. Yang, X. Huang, et al., Chem 6 (2020) 658–674.
[31] Y. Sun, L. Silvioli, N.R. Sahraie, et al., J. Am. Chem. Soc. 141 (2019) 12372–12381.
[32] E. Jung, H. Shin, B.H. Lee, et al., Nat. Mater. 19 (2020) 436–442.
[33] S.H. Yuan, A.P. Isfahani, T. Yamamoto, et al., Small Methods 4 (2020) 2000021.
[34] Z. Zhu, C. Chen, M. Cai, et al., Mater. Res. Bull. 114 (2019) 161–169.
[35] R. Liu, Q. Du, R. Zhao, et al., ChemCatChem 12 (2020) 3195–3201.
[36] J.W. Huang, Q.Q. Cheng, Y.C. Huang, et al., ACS Appl. Energy Mater. 2 (2019) 3194–3203.
[37] Y. Liu, X. Quan, X. Fan, H. Wang, S. Chen, Angew. Chem. Int. Ed. 54 (2015) 6837–6841.
[38] B. Feng, X. Wu, L. Li, et al., Chem. Eur. J. 25 (2019) 11560–11565.
[39] Y. He, H. Guo, S. Hwang, et al., Adv. Mater. 32 (2020) 2003577.
[40] Y. Wang, Y. Zhou, Y. Feng, X.Y. Yu, Adv. Funct. Mater. 32 (2022) 2110734.
[41] J. Yang, H. Liu, W.N. Martens, R.L. Frost, J. Phys. Chem. C 114 (2010) 111–119.
[42] A. Lenarda, M. Bevilacqua, C. Tavagnacco, et al., ChemSusChem 12 (2019) 1664–1672.